Webology (ISSN: 1735-188X)
Volume 18, Number 6, 2021

Study On The Creep Analysis, Ductility And Failure

Sandeep Kumar[1] , Dr. Milind Rohokale[2]

[1]Research Scholar, Department of Mechanical Engineering, Himalayan University, Itanagar, A. P.

[2]Research Supervisor, Department of Mechanical Engineering, Himalayan University, Itanagar, A. P.

ABSTRACT

Introduction: Structures are often a combination of bainite and ferrite for 1Cr-0.5Mo steel, mostly bainitic for 2.25Cr-1Mo steel, and totally martensitic for 9Cr-1Mo steel.

Aim of the study: the main aim of the study is to Study the creep analysis, ductility, and failure

Material and method: On the dissimilar weld junction as well as the base metals of P91 steel and 316LN SS, uniaxial tensile tests were performed. According to ASTM E8 standard, the specimen was produced and put through testing.

Conclusion: The findings of the standard creep test were used to properly verify the FEA model for creep damage, which indicated the potential for creep failure at the IC-HAZ.

1. INTRODUCTION

1.1 Physical Metallurgy of Cr-Mo Steels

Structures are often a combination of bainite and ferrite for 1Cr-0.5Mo steel, mostly bainitic for 2.25Cr-1Mo steel, and totally martensitic for 9Cr-1Mo steel. With increasing alloy concentration, the martensite start (Ms) temperatures rise to the 600s. From CCT data, we can ascertain that the Ms temperature for 2.25Cr-1Mo steel is near to 500°C, whereas for 3Cr-1Mo steels, it is approximately 450°C. Based on the TTT diagrams developed by Pickering and Vassiliou, the Ms temperature of 9Cr-1Mo steel is expected to be close to 400°C.

The sub-liquidus phase fields of a 9 wt. % Cr alloy include + -ferrite, +.-ferrite + carbides, and.-ferrite + carbides, depending on the temperature. The phase fields depicted in Fig. 1.8 are subject to change due to the presence of other alloying elements.

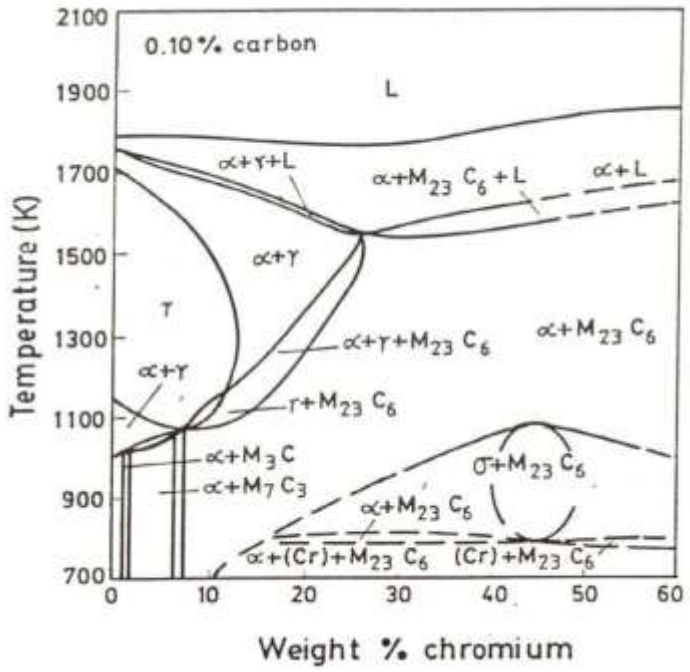

Fig. 1.1 Pseudo Binary Fe-Cr phase Diagram with 0.1 wt.%. Carbon

The tendency of high chromium ferritic steels to generate delta ferrite was predicted using this equation. Al, Ti, and N are not found in considerable amounts in P9 standard steel. These components' impacts on P9 steel were overlooked because of this assumption. To prevent austenite from being retained in the weld metal, nitrogen levels in this steel are continuously kept low.

2. LITERATURE REVIEW

Casalino (2019) has done pulsed Nd: YAG laser welding on surface harden steel alloy. The pulse width was most influenced parameter to promote surface hardness. The hardness could be improved laser scanning speed presence of harden laser layer ferrite phases. The high energy concentration was led to surface hardness of welded material. The laser hardened zone was revealed retained austenite phase with ferrite phase. The laser hardening was obtained highest hardness value as 673 VH compare to 572 VH in furnace hardening specimen. He was predicted the hardened region size and temperature profile by numerical model.

Moradi (2019) reported two different hardening process effects on stainless steel surface. The harden layer depth could be increased laser power and reducing speed of scanning. He was obtained maximum surface hardness as 630 HV and highest harden layer depth as 2.2 mm which was more than 90% from base material. The micro hardness deviation was high while applied laser power on surface of specimen. The high laser power and low scanning speed were ensured absence of ferrite phased. The laser diode laser hardening process was improved 1.4 times of hardness than the furnace hardening process. He was observed maximum impact energy and hardness as 630 HV, 35J and 380 HV, 35 J for laser hardening and furnace hardening process respectively.

Khorram (2019) has done research on surface hardening transformation on titanium alloy. The heat affected zone grain size; width and depth were increased by increasing laser pulse and laser speed. The laser beam welding overlapping factor was controlled to 96.9 % form 98.7 % by

increased speed of laser to 75 mm/min from 30 mm/min. He was observed significant overlapping as 95.2% at 105 mm/min laser speed. The harden zone was revealed alpha phase with beta grain prior. The rapid cooling process was forming martensite phase. The harden zone was shows transition region as alpha phase to beta phase. The optimum parameters were observed as 165 W power, 14 Hz frequency, 105 mm/min laser speed and 3.5 mm focus point.

Li (2019) applied strengthening mechanism on titanium laser welded specimens. He was analysis laser beam welding and hybrid laser beam welding with MIG welding process. The welded zones were revealed alpha grains with twin boundaries. The twin grains, acicular alpha grains and smaller grains were established strengthening of welded specimen. The MIG hybrid welded specimens was formed high concentration twin boundaries in heat affected zone and welded zone. He was concluded the MIG hybrid laser weld was produced better results.

Balanovskiy (2019) has done research on spot arc welding process influenced by surface hardening. He was investigating cathode spots influence on AISI 1060, 1050, 1020 and quenched steel for structure analysis and hardness. The heterogeneous structure was forming on specimen surface by ultra-high speed heating and cooling process. The specimen grain structure and grain size was refined significantly by applied surface hardening processing. The polycrystalline structure formation was observed in melted zone with signified grain size as 0.9 – 1.7 μm. The melt bath was found martensite structure on the grain boundaries.

3. METHODOLOGY

3.1 Mechanical Testing

3.1.1 Tensile test

On the dissimilar weld junction as well as the base metals of P91 steel and 316LN SS, uniaxial tensile tests were performed. According to ASTM E8 standard, the specimen was produced and put through testing. UTM testing apparatus type HT-2402 was used for the testing. For base metals, a circular bar specimen with dimensions of 5 mm in diameter and 25 mm in length was manufactured, and the test was run at room temperature with a 310-4 sec-1 strain rate. Table 3.1 contains the test matrix for the tensile test.

Table 3.1 Tensile testing-Test matrix

		No. of Specimen Tested
Base	**P91 Steel**	02
Metal	**316LN SS**	02

3.1.2 Automated ball indentation

The strength gradients at the corresponding HAZ and base metal of the dissimilar weld joints were examined using miniature specimen testing. The whole weld junction underwent testing. The tungsten carbide indenter is used in automated ball indentation (ABI) testing, which is seen in Fig. 3.1. The experiments were conducted using an indenter with a 0.25 mm diameter. The ABI tests were conducted on samples of 50105 mm in size at room temperature. As-welded, PWHT, and creep tested samples all underwent the tests. At each position, five loading and unloading cycles were performed while maintaining a consistent indentation depth. To remove

testing flaws and ensure that findings would be repeatable, each sample was tested three times.

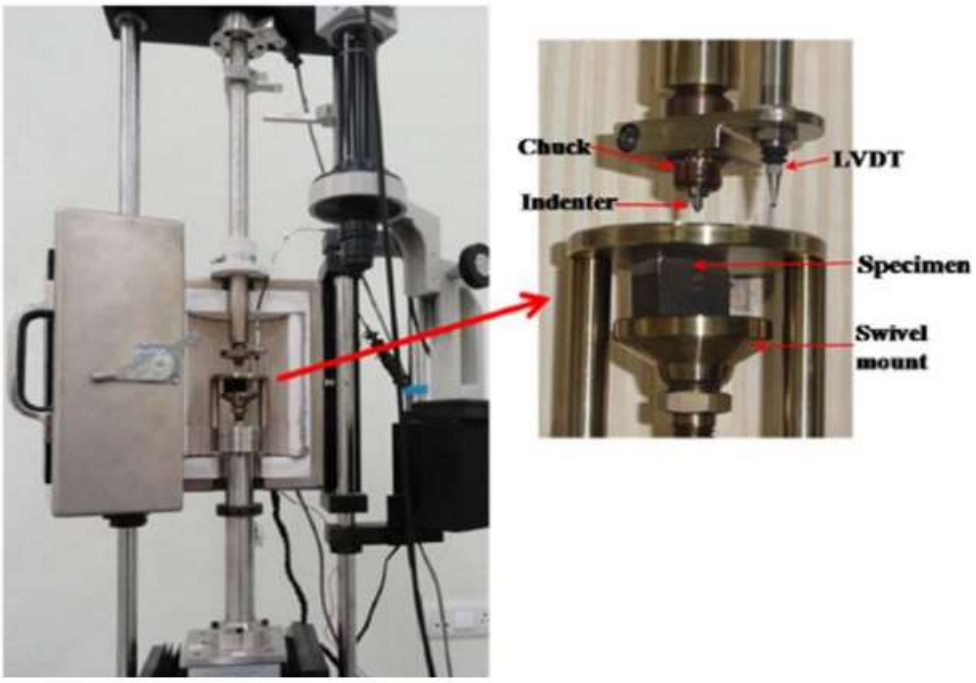

Fig. 3.1 ABI test setup

The Intercritical Heat Affected Zone (IC-HAZ), a microstructurally unique structure in the weld joint, had a minimum width of 0.85 millimetres. The indenter's size was selected such that different ABI results could also be achieved from this area. 30% of the indenter's diameter (0.035 mm) was the depth of the indentation. It was decided not to indent any deeper so as to protect the indenter.

3.1.2.1 ABI test-parameters

According to Fig. 3.2, the specimen was put through five cycles of loading and unloading as part of the ABI test. In each cycle, the material underwent elastic and plastic deformation.

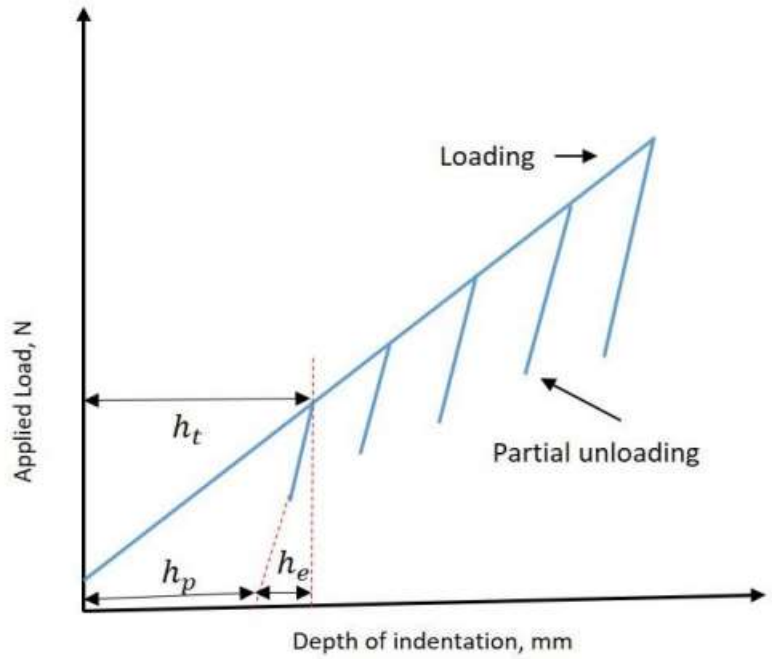

Fig. 3.2 Depth of indentation vs. applied load

Fig. 3.3 provides a graphic explanation of how ABI operates. During the loading cycle, a ball with a diameter of D indentations the specimen to a height, ht. After unloading, the height of the ultimate indentation, considering elastic recovery, remains to be calculated.

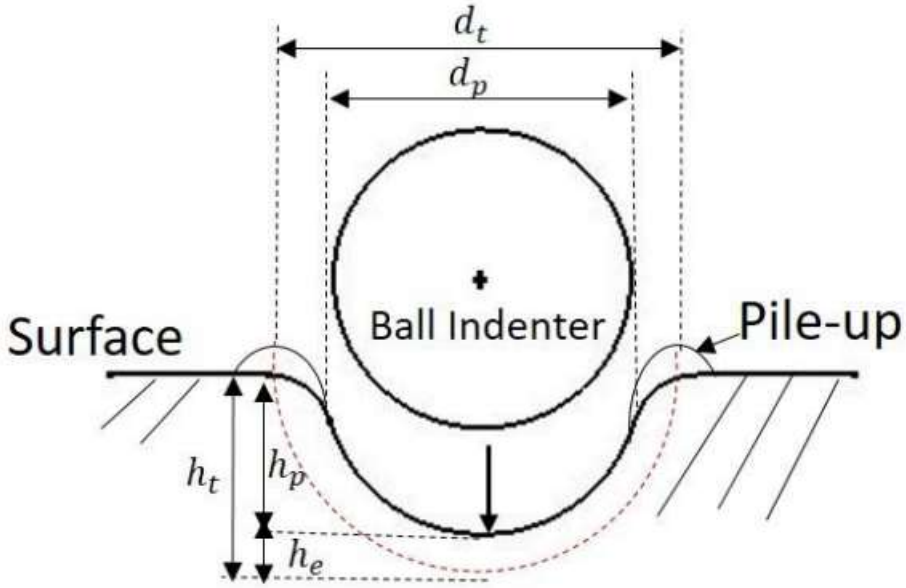

Fig. 3.3 ABI test parameters

3.1.3 Small punch creep test

The tiny punch creep test is a method of doing creep testing using a miniaturised disc specimen. A disc-shaped specimen with a diameter of 8 mm and a thickness of 0.5 mm was used in the experiment. The test was used to acquire the creep rate data pertaining to the localised areas of P91 steel heat-affected zone (HAZ). The experiment was conducted at a test temperature of 600 °C, using two different load levels for each heat-affected zone (HAZ) area and the P91 steel base metal. The test matrix conducted is shown in Table 3.2.

Table 3.2 Small punch creep-Test matrix

Load	**500 N**	**400 N**
P91 Base Metal	02 Specimens were tested at each load for all conditions at	
CG-HAZ		
FG-HAZ	**Temperature = 600 ºC**	
IC-HAZ		

4. RESULTS

4.1 Creep Data Analysis

4.1.1 Stress-rupture curve

Two test temperatures were used to create the S-R curve, which shows the relationship between rupture life and stress intensity. In Fig. 4.41 below, it is shown. Due to the severity of the temperature speeding the damaging events, as will be mentioned later, the rupture life achieved at 600 ^{o}C was lower than that obtained at 550 ^{o}C.

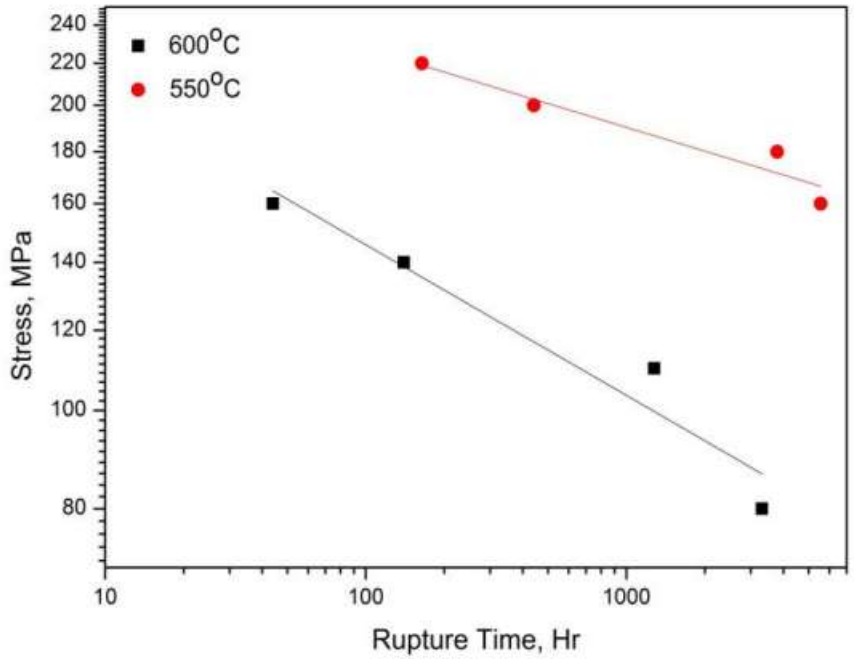

Fig. 4.1 S-R curve for dissimilar weld joint at two test temperature

4.1.2 Minimum creep rate curve

Table 4.8 displays the minimal creep rate assessed at both test temperatures and their corresponding stress levels. Fig. 4.42 shows the graph produced by plotting the minimal creep rate versus applied stress for both temperatures using the data.

Table 4.1 Minimum creep for creep test at 550 ℃ and 600 ℃

Temperature 550 ℃		**Temperature 600** ℃	
Stress (MPa)	**Minimum creep rate (/h)**	**Stress (MPa)**	**Minimum creep rate (/h)**
220	2.73×10^{-4}	**160**	1.31×10^{-3}
200	1.19×10^{-4}	**140**	3.02×10^{-4}
180	3.25×10^{-5}	**110**	3.53×10^{-5}
160	7.87×10^{-6}	**80**	6.07×10^{-6}

Norton's equation is often followed by the minimum creep rate curve, as seen below:

$$\varepsilon'_{min} = A\sigma^n \quad (4.4)$$

where ' εmin is The minimal creep rate may be represented by the variables σ, n, and A, where σ is the applied stress, n represents the stress exponent, and A corresponds to Norton's constant.

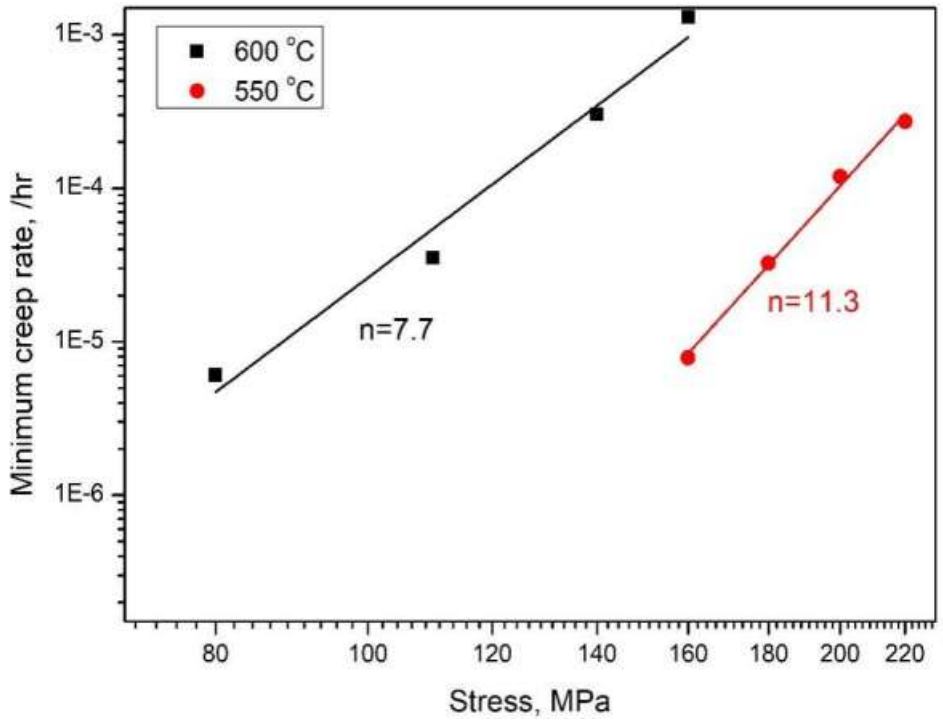

Fig 4.2 Minimum creep rate vs. stress

The values for the parameters, n and A, were derived from the slope and y-intercept seen in the line graph shown in Figure 4.1. These values are documented in Table 4.2. The observed values at their corresponding temperatures were found to be consistent with the values of the P91 material.

Table 4.2 Norton's Law constants at test temperatures

Temperature (℃)	**Norton's Law Constant**	
	n	**A (MPa^{-n}/h)**
550	11.3	2.16×10^{-9}

600	7.7	9.79×10^{-14}

Both the parameters n and A play a vital role in the analysis of creep damage in weld joints. The value of n decreased as the creep temperature increased. During the process of creep exposure at the specified test temperatures, the deformation was seen to be primarily driven by both diffusion and dislocation motion mechanisms.

The estimation of the value of n allowed for the determination of the variation in creep deformation mechanism resulting from the two different test temperatures. At a temperature of 550 ºC, the observed value of 11.3 suggests a decrease in dislocation climb deformation, resulting in slower diffusion. Conversely, at an increased temperature of 600 ºC, the value of 7.7 indicates a quick diffusion process characterised by dislocation glide type of creep deformation.

4.1.3 Creep ductility

The measure of creep ductility may be quantified using two parameters: the percentage decrease in cross-sectional area (% RA) and the percentage elongation (% el.). Figures 4.3 (a) and (b) depict the graphical representations of the relationship between the percentage of RA and the percentage of el. about rupture time, respectively. The percentage of relative area (RA) was quantified at the site of fracture. In Figure 4.43 (a), it was observed that the percentage of RA decreased from about 90% (at a pressure of 220 MPa) to 60% (at a pressure of 160 MPa) when the test temperature was set at 550 ℃. The rise in test temperature had little impact on the percentage of relative abundance (%RA). At a test temperature of 600 ℃, the percentage of reduction in the area fraction of recrystallized grains (% RA) decreased when the applied stress was lowered from 160 to 80 MPa. At greater stress levels, the percentage was almost 90%, but at lower stress levels, it was a mere 15%. The observed decrease in the percentage of RA (reduction in area) at a pressure of 80 MPa and a temperature of 600 ℃ may be attributed to the manifestation of a brittle Type-IV failure.

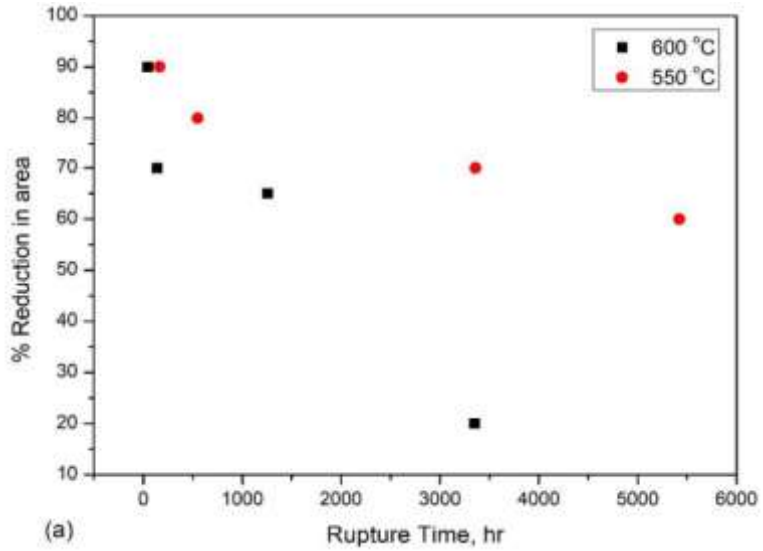

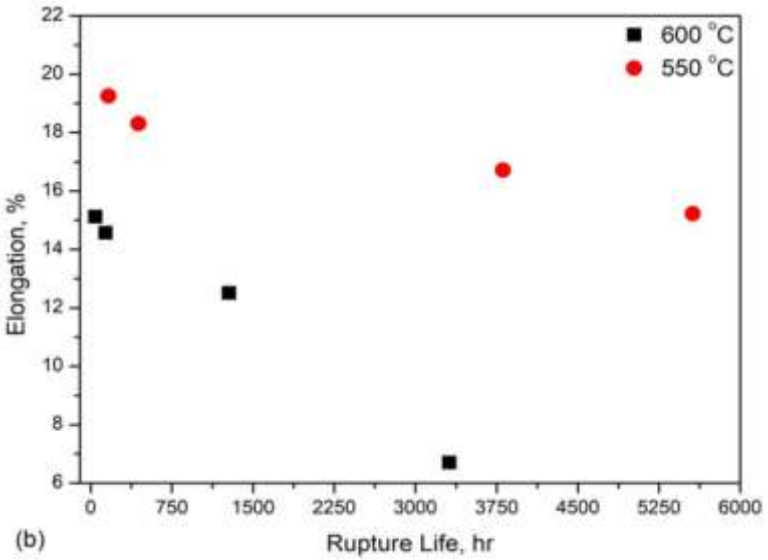

Fig. 4.3 (a) % Reduction in area curve (b) Percentage Elongation during creep exposure

Like the percentage of RA, the percentage of el. likewise exhibited a same pattern. In Figure 4.3 (b), the percentage of elongation (% el.) was seen to be maximum at around 16% for both higher applied stresses of 160 and 140 MPa, when the temperature was 600 ℃. Conversely, the lowest percentage of elongation was recorded at 6.7% for an applied stress of 80 MPa. An observation was made about the greatest elongation, which measured 18.85%, at a stress level of 220 MPa and a test temperature of 550 ℃. It was noted that there was a little variation in elongation, with a minimum value of 15%, when the stress level was reduced to 160 MPa.

It was noticed that there was a decrease in the percentage of reduction in area (% RA) and percentage of elongation (% el) as the rupture life increased at both temperatures. This finding indicates a decrease in creep ductility as the rupture life progresses. At a temperature of 550 ºC, the influence of temperature on the ductility of creep, as assessed by the percentage of reduction in area (% RA) at higher stress levels ranging from 180 to 220 MPa, is minimal. Nevertheless, the impact of test temperature on creep ductility was significant at stress levels of 160 MPa or below. The findings indicate that there is a correlation between higher values of % RA (ranging from 90% to 60%) and moderate values of % el. (ranging from 18% to 12%) at elevated stress levels of 220-160 MPa. This suggests that there was a fast concentration of creep deformation near the failure zone, and the ultimate rupture mostly took place by ductile mechanisms. The failures exhibited ductile behaviour despite the high amounts of stress. At a lower stress level of 80 MPa and a temperature of 600 ºC, the percentages of reduction in area (% RA) and elongation (% el.) were observed to be 15% and 6.7% respectively. This observation suggests that no ductile failure had place during the exposure to creep. The percentage of elongation (el) exhibited the lowest value among all measurements at the given test temperature, suggesting the absence of a brittle failure mechanism. The failure mode will be further examined in the subsequent section.

4.2 Creep failure

The failure of dissimilar weld joints was seen in the P91 base metal, across most stress levels at both test temperatures. A Type-IV failure, which conforms to the usual characteristics of this failure mode, was seen under creep conditions at a temperature of 600 ºC and a stress level of

80 MPa. A comprehensive analysis of this failure is provided. The occurrence of creep failure was seen in the base metal of P91 for a specific specimen, as shown in Figure 4.44, where the conditions of 600 ºC and 160 MPa were applied. An observation was made of a cup and cone fracture with ductile characteristics, which was shown to be connected with a second necking phenomenon within the heat-affected zone (HAZ) of P91 steel. A cross-sectional sample was obtained by bisecting the centre portion of the specimen, revealing distinct evidence of dual necking. This is shown by the dotted line in Figure 4.4.

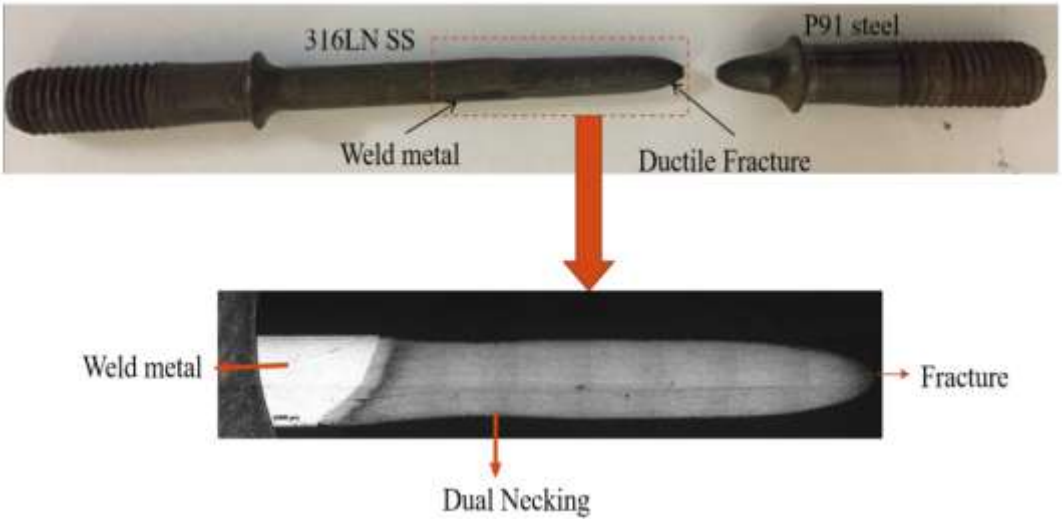

Fig. 4.4 Cross-section of creep fractured specimen

The occurrence of dual necking was seen in almost all of the samples that experienced failure in the P91 base metal. This phenomenon has been previously documented and may be attributed to the accumulation of stress in the most vulnerable heat-affected zone (HAZ) area due to inconsistencies in its microstructure. During the process of creep exposure, the combination of temperature and applied uniaxial loading results in the development of a triaxial condition of stress inside the P91 heat-affected zone (HAZ) area.

5. CONCLUSION

The findings of the standard creep test were used to properly verify the FEA model for creep damage, which had indicated the potential for creep failure at the IC-HAZ. The results of miniaturised specimen creep tests and conventional creep tests were correlated, and SPC was verified. Interrupted creep experiments were helpful in determining how cavitation developed in the P91 steel HAZ during creep, revealing that the tertiary regime was the only time when creep cavities began to form

REFERENCES

1. Balanovskiy, AE 2019, ‘Surface hardening of structural steel by cathode spot of welding arc,’ IOP Conference Series: Materials Science and Engineering. vol. 560, no. 1. IOP Publishing.
2. Casalino, Giuseppe 2019, ‘Experimental and numerical study of AISI 4130 steel surface hardening by pulsed Nd: YAG laser,’ Materials vol.12 (19), pp.3136.
3. Khorram, Ali, Akbar DavoodiJamaloei &Abed Jafari 2019, ‘Surface transformation

hardening of Ti-5Al-2.5 Sn alloy by pulsed Nd: YAG laser: an experimental study,' The International Journal of Advanced Manufacturing Technology vol. 100, no.9-12, pp. 3085-3099.
4. Moradi, Mahmoud, HosseinArabi & Alexander FH Kaplan 2019, 'An experimental investigation of the effects of diode laser surface hardening of AISI 410 stainless steel and comparison with furnace hardening heat treatment,' Journal of the Brazilian Society of Mechanical Sciences and Engineering vol. 41, no.10,p. 434.
5. Olanipekun, AyorindeTayo, Nthabiseng Beauty Maledi & Peter MadindwaMashinini 2020, 'The synergy between powder metallurgy processes and welding of metallic alloy: a review,' Powder Metallurgy vol.63, no.4,pp. 254-267.
6. Palán, J, Kubina,T & Motyčka,P2017, 'The effect of annealing on mechanical and structural properties of UFG titanium grade 2,' IOP Conference Series: Materials Science and Engineering. vol. 179. no. 1. IOP Publishing.
7. Palanivel, R, Dinaharan,I & Laubscher,RF2017, 'Microstructure evolution and mechanical characterization of Nd: YAG laser beam welded titanium tubes,' Materials Characterization vol.134, pp.225-235.
8. Panwisawas & Chinnapat 2017, 'Keyhole formation and thermal fluid flow-induced porosity during laser fusion welding in titanium alloys: Experimental and modelling,' ActaMaterialia vol. 126, pp. 251-263.
9. Park, Young Whan & Sehun Rhee 2008, 'Process modeling and parameter optimization using neural network and genetic algorithms for aluminum laser welding automation,' The International Journal of Advanced Manufacturing Technology vol.37, no.9-10, pp.1014-1021.
10. Paul & Alexander 2017, 'Hot metal gas forming of titanium grade 2 bent tubes,' AIP Conference Proceedings. Vol. 1896. No. 1. AIP Publishing LLC.